Epitaxial thin film of high entropy oxide as electrocatalyst for oxygen evolution reaction

Ranjan Kumar Patel,[1,*] Ramesh Naidu Jenjeti,[2,*] Rajat Kumar,[2] Nandana Bhattacharya,[1] C. Klewe,[3] P. Shafer,[3] S. Sampath,[2,†] and S. Middey[1,‡]

[1]*Department of Physics, Indian Institute of Science, Bengaluru 560012, India*

[2]*Department of Inorganic and Physical Chemistry, Indian Institute of Science, Bengaluru 560012, India*

[3]*Advanced Light Source, Lawrence Berkeley National Laboratory, Berkeley, California 94720, USA*

Abstract

High entropy oxides (HEOs), which contain multiple elements in the same crystallographic site, are a promising platform for electrocatalysis in oxygen evolution reaction (OER). However, to date, all OER studies involving HEOs have used it in polycrystalline bulk form. In this study, the OER activity of a set of single crystalline thin films of ($La_{0.2}Pr_{0.2}Nd_{0.2}Sm_{0.2}Eu_{0.2}$)$NiO_3$, grown on $NdGaO_3$ substrates have been investigated. The OER activity increases with the thickness of the film. X-ray absorption spectroscopy measurements find an increase in Ni d-O p covalency and a decrease in charge transfer energy with the increase in film thickness. These facilitate higher charge transfer between Ni and surface adsorbates, resulting in higher OER activity. However, the epitaxial stabilization of thicker film becomes difficult due to the requirement of +3 oxidation state of Ni and the OER activity of a 75 unit cell thick film is found to be the optimal in the present study. This work demonstrates that the thickness of perovskite oxides can be used as a parameter to enhance OER activity.

* Contributed equally

† sampath@iisc.ac.in

‡ smiddey@iisc.ac.in

I. INTRODUCTION

General consciousness about issues like global warming, depletion of fossil fuel resources, etc., have fostered massive efforts in energy research in the 21st century. Oxygen evolution reaction (OER) is a key process in several alternative energy generation platforms such as solar [1] and electric [2, 3] driven water splitting, fuel cells [4], rechargeable metal-air batteries [5, 6], etc. However, the commercially available catalyst for OER is based on 4d/5d transition metal oxides (RuO_2, IrO_2) [7–9], which involves higher costs and poor long-term stability. To avoid these issues, there have been significant efforts with 3d transition metal oxides (TMO), where electronic structure parameters are being used as descriptors to obtain superior catalysts [10–14]. Epitaxial stabilization of TMOs has added a new dimension to this field as it allows finding an intrinsic catalytic activity without the effect of grain boundaries, defects, etc [15, 16]. Moreover, the heterostructure route allows tuning of the electronic activity descriptors using the same material [17–26].

Parallelly, the synergetic development of ab-initio theoretical methods, materials prediction by machine learning, progress in materials growth methods, and nanoscale materials characterization techniques have enabled the community to explore new families of transition metal oxides. One such rapidly developing class of materials is based on high entropy oxides (HEOs), where multiple elements, generally five or more, occupy the same crystallographic site in equiatomic or near equiatomic ratios [27]. The implementation of such HEOs for OER is a promising avenue as the HEO allows access to unexplored regions of complex phase diagrams. However, this field is at its infancy and all the efforts so far have used HEOs in polycrystalline, bulk form [28–36]. While investigating OER with epitaxial films of HEO is certainly the next logical step, such studies are completely missing so far, most likely due to the difficulty of thin-film growth of such multi-component systems in single crystalline form.

To explore the electrocatalysis activity of HEO in thin film geometry, we consider the family of RENiO$_3$ (RE = La, Pr, Nd, Sm, Eu.....Lu) [37–40]. Bulk LaNiO$_3$ [Ni^{3+}: t_{2g}^6, e_g^1 (pure ionic picture)] remains metallic and rhombohedral to the lowest temperature. Bulk RENiO$_3$ with RE=Pr, Nd undergoes a simultaneous metal to insulator transition (MIT), a magnetic transition (paramagnetic to antiferromagnetic), and a structural transition (orthorhombic to monoclinic) around 135 K, 215 K, respectively. Bulk SmNiO$_3$ and EuNiO$_3$ exhibit MIT around 400 K and 460 K, respectively, accompanied by a structural symmetry change while the antiferromagnetic insulating phase appears around 225 K and 205 K, respectively. This coherent increase in the MIT temperature with

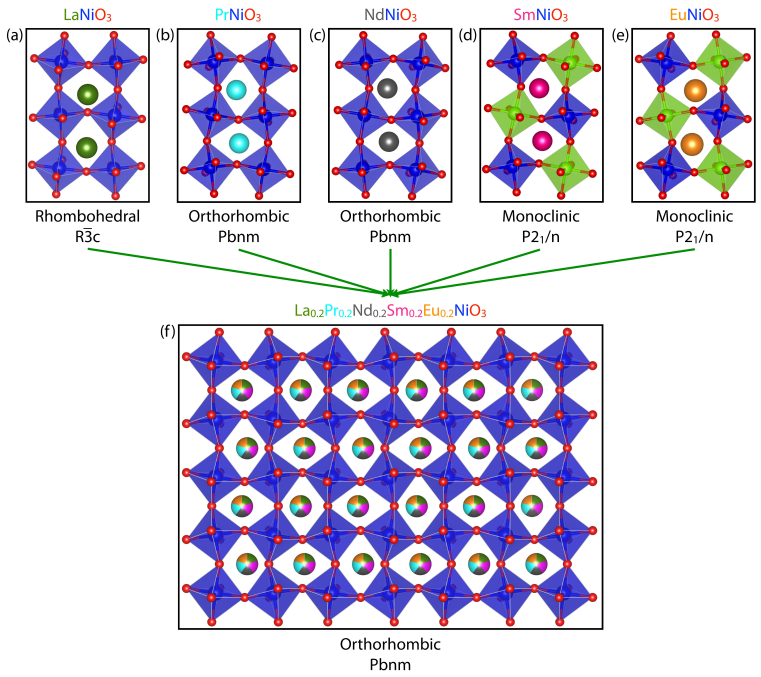

FIG. 1. **Schematic structure of the bulk HEO.** (a)-(e) Structure of bulk $LaNiO_3$, $PrNiO_3$, $NdNiO_3$, $SmNiO_3$, and $EuNiO_3$, respectively at room temperature. $LaNiO_3$ is rhombohedral with one kind of Ni. $PrNiO_3$ and $NdNiO_3$ are orthorhombic in nature, having a single type of Ni. $SmNiO_3$ and $EuNiO_3$ exist in monoclinic structure and there are two types of Ni arranged in alternating fashion in all three directions. (f) A schematic of the HEO possessing orthorhombic symmetry at room temperature having one type of Ni. The RE site atoms (La, Pr, Nd, Sm, and Eu) can occupy any A site of the HEO perovskite with equal probability.

the decrease in RE-ion radius is attributed to the distortion of NiO_6 octahedra, specifically to the reduction in Ni–O–Ni bond angles [41]. OER activity of several members of the $RENiO_3$ series have been studied recently in thin film form [19–23]. The splitting between two e_g orbitals, formation of defects, and compressive strain are found to be favorable for OER [19, 20]. Hole doping and application of pressure also enhance the OER activity [21, 22]. Surprisingly, the investigation of the OER activity of nickelate perovskites as a function of the film thickness is missing even though the strength of various descriptors are strongly dependent on the film thickness [42–45]. On the other hand, the stabilization of thicker nickelate films is challenging and very often, it leads to phase decompositions [46], which will have also effect on electrocatalysis. Another interesting and challenging problem to address would be how the OER activity evolves when several members of this $RENiO_3$ series are combined to form a HEO composition. Very recently, we have

been able to stabilize such a compound, $(La_{0.2}Pr_{0.2}Nd_{0.2}Sm_{0.2}Eu_{0.2})NiO_3$ [(LPNSE)NO] in single crystalline form [47] (see Fig. 1), providing us the opportunity to explore both of these aspects.

In this work, we have investigated OER electrocatalytic activity of 15 uc, 30 uc, 45 uc, 75 uc and 100 uc thin films of (LPNSE)NO (uc= unit cell in pseudocubic setting). These single crystalline films were grown in layer-by-layer fashion by pulsed laser depsition and the films have been characterized by reflection high energy electron diffraction (RHEED), X-ray diffraction (XRD), and electrical transport measurements. The RHEED images demonstrate that the films are 2D up to 75 uc and develop a quasi-3D character for higher thickness. The XRD patterns testify single crystallinity of all the films, whereas the transport measurements show all (LPNSE)NO films undergo a first order metal to insulator transition with a thermal hysteresis. Comprehensive OER measurements were done on all the HEO thin films and 75 uc film is found to be the best eletrocatalyst among all films investigated here. Ni $L_{3,2}$ and O K edges XAS (X-ray absorption spectroscopy) measurements demonstrate that the enhancement of OER activity is intimately connected with electronic structure parameters (charge transfer energy between Ni d and O p states and Ni-O covalency).

II. RESULTS AND DISCUSSION

A. Growth and structural characterization

We have grown a series of (LPNSE)NO thin films with varying thicknesses on single crystalline $NdGaO_3$ $(1\ 1\ 0)_{\rm or}$ substrates [= $(0\ 0\ 1)_{\rm pc}$, or and pc denote orthorhombic and pseudo-cubic setting respectively] by a pulsed laser deposition unit, connected with a RHEED (reflection high energy electron diffraction) set up. Synthesis of bulk $RENiO_3$ requires high pressure as Ni has an unusual +3 oxidation state. In spite of all attempts, large single crystals have been grown only for $LaNiO_3$ [48] and $PrNiO_3$ [49] so far. The stabilization of the single-crystalline phase of (LPNSE)NO in thin film form without high oxygen pressure can be understood by considering a model by Kaul $et\ al.$ [50], where the relative difference between the free energies for the bulk and epitaxially stabilized phases is given by

$$\Delta E = \Delta E^{ic} - \Delta E^{c} = d[\Delta G_v^{ic} - \Delta G_v^{c} - \frac{\mu}{1-\nu}\epsilon^2] + [\sigma_s^{ic} - \sigma_s^{c}] \quad (1)$$

Here, the superscripts ic and c represent the epitaxially incoherent (free from substrate) and coherent phases, respectively. d denotes the film thickness and ΔG_v is the Gibbs free energy per

unit volume. μ and ν are the shear modulus and Poisson's ratio, respectively. The relative lattice mismatch between the unit cell parameters of the substrate and the desired phase is denoted by ϵ and the surface tension is represented by σ_s. The 2^{nd} term of the above Equation 1 is always positive, which is the surface contribution, whereas the 1^{st} term remains negative (volume term). To stabilize an epitaxially coherent phase, $\Delta E > 0$. Moreover, as per Equation 1, there may be a phase decomposition (i.e. RE_2O_3 and NiO) with the increase in film thickness (d) or the lattice mismatch (ϵ).

In this paper, (LPNSE)NO films with thicknesses 15 uc, 30 uc, 45 uc, 75 uc and 100 uc (uc= unit cell in p.c. setting) have been investigated. All of the growths were carried out in a PLD system at 735°C with a dynamic oxygen pressure of 150 millitorr [47]. During the growing process, an excimer laser with a fluence of 1.5 Jcm^{-2} was used. Following the growths, the samples were post-annealed for 30 minutes at the growth temperature under a 500 torr oxygen pressure before being cooled to ambient temperature. The RHEED pattern of NGO $(1\ 1\ 0)_{\rm or}$ substrate consists of very sharp specular (0 0) and off-specular (0 $\pm$1) Bragg spots (Fig. 2(a)), which are very typical for an infinite crystal with a very smooth surface. For each thin film, we have monitored the progress of the growth by recording the variation of the intensity of the specular spots of the RHEED pattern and Fig. 2(b) displays such a RHEED oscillation pattern during the growth of a (LPNSE)NO thin film, confirming the desired layer-by-layer growth of the film. Fig. 2(c), (d) represent RHEED images after cooling the 15 uc and 75 uc samples to room temperature, respectively. The streaky pattern of the specular (0 0) and off specular (0 $\pm$1) spots establishes that we have been able to maintain two-dimensional nature of the film with very smooth surface morphology even in the 75 uc (LPNSE)NO film. However, we have observed broken streaks in the RHEED pattern of the 100 uc film (Fig. 2(e)), signifying development of quasi 3D nature of the film surface. Hence, we have restricted the thickness dependent OER study up to 100 uc thick film.

To confirm epitaxial growth, we have performed X-ray diffraction (XRD) measurements of all films. Fig. 2(f) shows XRD pattern around the $(002)_{\rm pc}$ reflection of $NdGaO_3$ substrate. The single crystallinity of all the films were confirmed by the broad film peak (denoted by *) in the vicinity of the sharp substrate peak. In addition, the presence of well defined Kiessig fringes confirm high structural quality of all these films. The out of plane lattice constant ($c_{\rm pc}$) of these 15 uc, 30 uc, 45 uc, 75 uc and 100 uc (LPNSE)NO films are found to be 3.8 Å, 3.792 Å, 3.784 Å, 3.788 Å, 3.798 Å, respectively. The film thickness, evaluated from the separation of the Kiessig fringes is very close to the expected value from the number of RHEED oscillations multiplied by $c_{\rm pc}$.

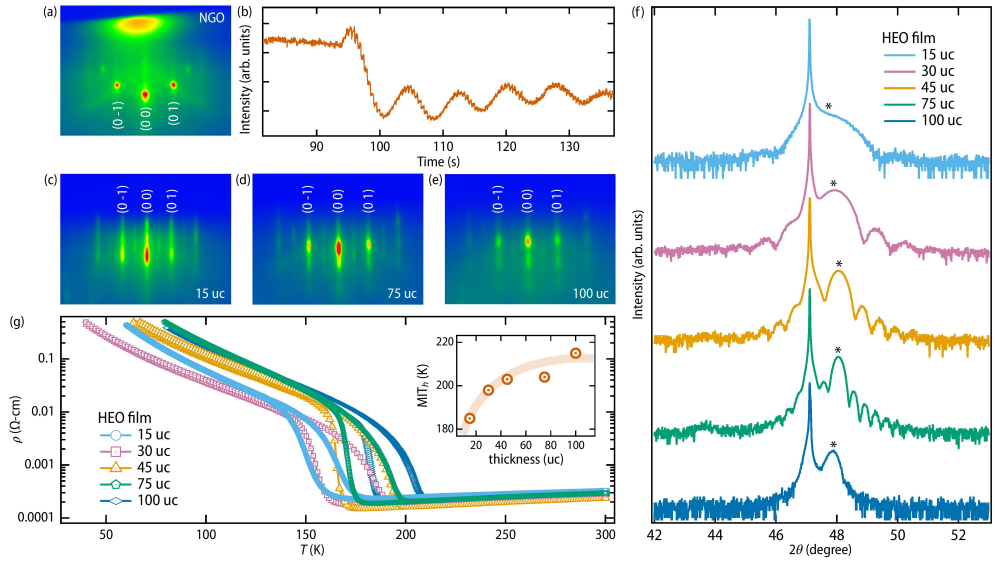

FIG. 2. **Structural and electrical characterization.** (a) RHEED image of the single terminated NGO $(1\ 1\ 0)_{\rm or}$ substrate. (b)The change in the intensity of the specular spot with time of a (LPNSE)NO film during the growth. (c)-(e) The RHEED image of the 15 uc, 75 uc, and 100 uc samples after cooling to room temperature. (f) 2θ-ω XRD scan around $(002)_{\rm pc}$ peak of the NGO substrate for all the thin films. (g) Temperature dependent resistivities of the (LPNSO)NO films. The metal to insulator transition temperature in the heating run as a function of the thickness has been shown in the inset of (g). The XRD and transport data for 30 uc and 45 uc thin films have been reproduced with permission[47] 2020, Appl. Phys. Lett.

B. Electrical characterization

To check the electronic transport properties, resistivity is measured as a function of temperature for this series of (LPNSE)NO films (Fig. 2(g)). All of the films undergo first order MIT with a thermal hysteresis and the hysteresis is known to be arises due to the coexistence of insulating and metallic domains [51, 52]. The 100 uc sample shows a very sharp MIT ($T_{\rm MIT}$ $\sim$ 218 K in the heating run) and the $T_{\rm MIT}$ shifts towards lower temperature with the decrease in the film thickness (inset of Fig. 2(g)). A similar trend has already been observed for $NdNiO_3$ thin films and is related to the epitaxy and finite thickness [53–55]. It may be noted here that some earlier work has demonstrated that the OER activity of RENiO$_3$ thin films are also affected by oxygen vacancies [23]. We would like to emphasize that the resistivity of all thin films investigated in this present work are very similar at room temperature, implying oxygen vacancies, if present, should be of a similar order in all cases [56].

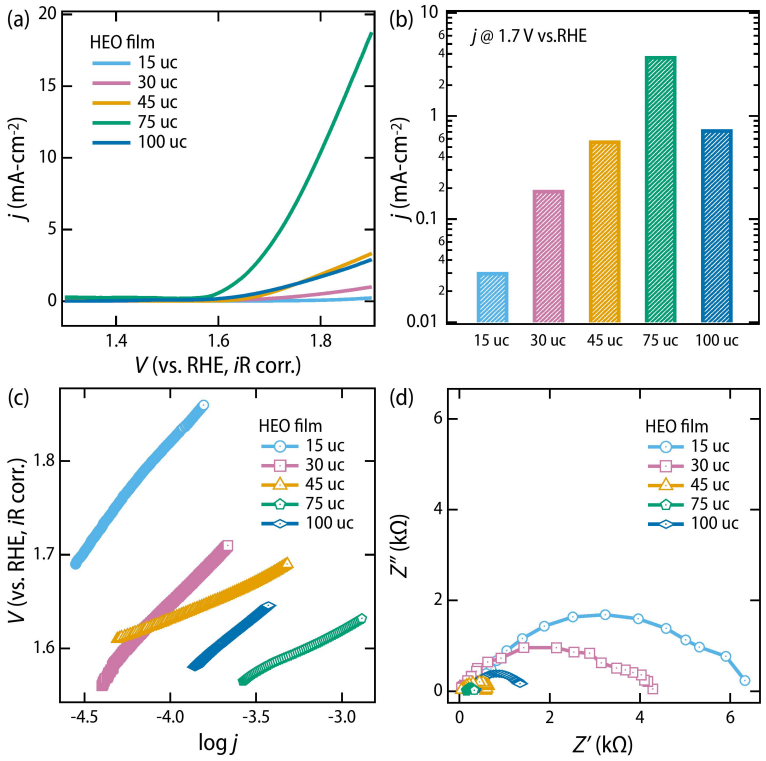

FIG. 3. **Oxygen evolution reaction of HEO thin films.** (a) LSV curve of (LPNSE)NO thin films with different thicknesses in 0.1 M KOH electrolyte, normalized by the exposed areas with voltage corrected for the resistance of the electrolyte. (b) Comparison of OER catalytic activity, defined by the current density obtained at 1.7 V vs. RHE of the OER overpotential and thickness of the films. The y-axis is in the log scale. (c) Tafel slopes and (d) electrochemical impedance spectra of the corresponding (LPNSE)NO films.

C. Oxygen evolution reaction

After competent structural and electrical characterization of the (LPNSE)NO thin films, we investigate the impact of thickness on the oxygen evolution reaction (OER) activities. All the (LPNSE)NO thin films were electrically contacted at one corner of the front side and a standard three electrode configuration: (LPNSE)NO film as working, Mercury-mercuric oxide (MMO) as the reference, and carbon rod as the counter electrode, were used to measure the OER activity in 0.1 M KOH (potassium hydroxide) solution. Fig. 3(a) shows the iR-corrected LSV (linear-scan voltammetry) curves for (LPNSE)NO films with varying thicknesses. The onset potentials are very similar (see Table I) for all of these films. In general, specific activity [current density (j) at a particular potential V vs. RHE (reversible hydrogen electrode) is used to compare the OER activity more clearly. Here, we have compared the j at 1.7 V vs RHE in the Fig. 3(b), which

TABLE I. **Summary of OER electrocatalytic data**

thickness	onset potential (V vs RHE)	Tafel slope (mVdec^{-1})	j @1.7 V (μAcm^{-2})	R$_C$T (Ohms)
15 uc	1.60	226	31	6169
30 uc	1.55	194	192	4428
45 uc	1.59	81	580	668
75 uc	1.56	90	3816	330
100 uc	1.60	150	745	1332

demonstrates an increase of j with film thickness up to the 75 uc thick film. Interestingly, the current density is much lower for 100 uc film compared to the 75 uc one. Our detailed post-OER sample characterizations (Fig. S2) revealed the degradation of the 100 uc film under an electrolysis environment. We attribute this to the lower stability of thicker (LPNSE)NO film, as inferred from Equation 1.

To investigate OER kinetics, Tafel slopes have been calculated by plotting the potential as a function of log (j) and taking the slope of it (Fig. 3(c)). The Tafel slope decreases from 226 mVdec^{-1} to 90 mVdec^{-1} with the increase of film thickness from 15 uc to 75 uc (Table I), implying an accelerated OER kinetics in 75 uc film. This is further supported by electrochemical impedance spectroscopy (EIS) measurements. The charge transfer resistances (R_{ct}) were calculated by fitting the Nyquist plots (Fig. 3(d)), and a decrease of R_{ct} to 330 Ω for 75 uc film is observed (R_{ct} is 6169 Ω for the 15 uc film). The summary of all the data of the electrocatalytic measurements are shown in Table I. From all these analyses, it is evident that the thickness of these samples follows a volcano shaped OER activity trend, with the 75 uc (LPNSE)NO thin film seeming to be the best candidate among the films investigated in this work.

D. X-ray absorption spectroscopy

In order to understand the enhancement of OER activity as a function of film thickness, we focus on electronic structure parameters. The electronic structure of complex oxides is generally described by electron hopping strength (t), electron-electron correlation (U), and charge transfer energy (Δ) within the scheme of the Zaanen-Sawatzky-Allen (ZSA) phase diagram [57, 58] . The separation between the lower Hubbard band (LHB) and the upper Hubbard band (UHB) is defined

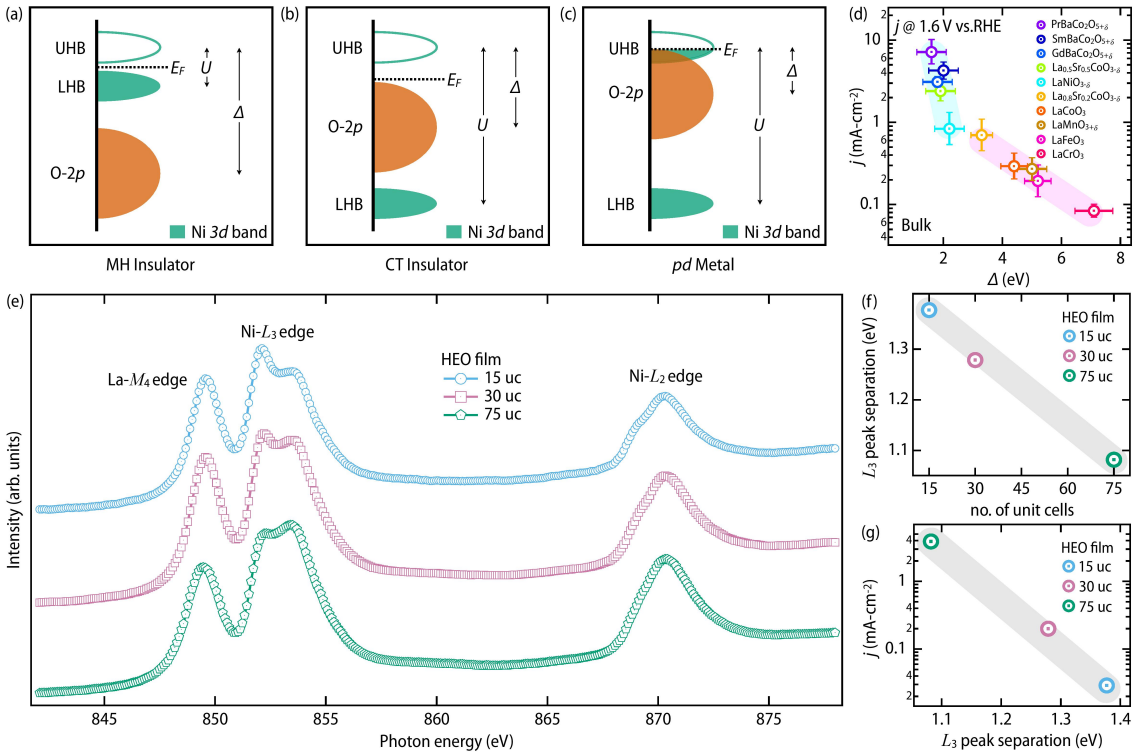

FIG. 4. **Ni L-edge X-ray absorption spectroscopy.** (a)-(c) A schematic density of states representation of the Mott-Hubbard (MH) insulator ($U<\Delta$), Charge Transfer (CT) insulator ($U>\Delta$), and pd metal, respectively. The HEO at room temperature belongs to the pd metal. (d) The relation between the activity of some bulk material (in terms of current density) and Δ are listed, showing a linear kind of trend. The data set has been reproduced with permission[11] 2017, Energy Environ. Sci. (e) Ni $L_{3,2}$-edge XAS spectra for 15, 30, and 75 uc (LPNSE)NO films. The peak around 849 eV arises due to La M_4-edge. (f) The energy separation between the two peaks of the Ni L_3-edge as a function of the thickness of the films. (g) The current density as a function of the energy separation between the two peaks of the Ni L_3-edge, which is a measure of Δ. The y-axis is in the log scale.

as U, whereas the separation between the UHB and the O $2p$ is interpreted as Δ. In accordance to the ZSA phase diagram, there are several ground states like Mott-Hubbard (MH) insulator, charge transfer (CT) insulator, d metal or pd metal (Fig. 4(a)-(c)). For MH insulator, where $U<\Delta$, the O $2p$ lies below the LHB in the energy band diagram and the band gap is mainly controlled by U. On the other hand, Δ primarily controls the bandgap in the case of CT insulator as $U>\Delta$. In the case of a pd metal, the UHB overlaps with the O $2p$ band. The electronic state of our (LPNSE)NO films at room temperature belongs to this pd metal phase [59]. In recent years, the trends in OER activity

of transition metal oxides are often described by different electronic structure parameters like the occupancy of the e_g* orbital of the B site of ABO_3 perovskite, Δ and the covalency between $2p$ and $3d$ orbital of the O and B sites, respectively. For example, the activity pattern of several perovskite oxides follow a volcano shaped relation with the occupancy of the e_g* orbital and the materials with nearly 1 electron in the e_g* orbital shows maximum OER activity [10, 12, 60]. Furthermore, the OER activity increases with increase in the covalency [10, 20, 22, 23] or by decreasing the charge transfer energy of the materials [22]. Interestingly, Hong et al. [11] have emphasized that Δ is enough to understand the trends in the OER activities of the oxide materials without considering the e_g* occupancy, in contrary to previous study [10]. The dependence of OER activity of different compounds in their bulk form available in the literature [11] with the corresponding Δ has been shown in Fig. 4(d), which clearly shows strong dependence of j on Δ. Interestingly, the current density decreases sharply with the increase Δ for $\Delta < 2$ eV, whereas the decrease is more gradual in the higher Δ regime. This might be related to the fact that the electronic structure in $U < \Delta$ regimes (MH insulators and d metals) is controlled by U, whereas Δ is the determining factor in the $U > \Delta$ region (CT insulators and pd metals) [39].

While a d^7 electronic configuration of Ni^{3+} is expected in rare-earth nickelate from a pure ionic picture, the ground state, in reality, consists of d^7 and $d^8\underline{L}$ configurations due to strong hybridization and negative Δ [61, 62]. To investigate how the OER activity is linked to the electronic structure details for our (LNPNSE)NO thin films, we have measured XAS at the Ni $L_{3,2}$-edges at 300 K in bulk sensitive TFY (total fluorescence mode). In Ni XAS, an electron either from the completely filled Ni $2p_{1/2}$ or $2p_{3/2}$ state absorb the energy from the X-ray and goes to a partially filled Ni $3d$ state, giving rise to Ni L_2 and L_3 edges, respectively. Ni XAS spectra for the 15 uc, 30 uc and 75 uc films are shown in Fig. 4(e), which confirms desired +3 oxidation state of Ni. Although there is a strong overlap between the La M_4-edge (around 849 eV) and Ni L_3-edge (around 853 eV), double peak feature of the Ni L_3-edge is quite prominent. The decrease in the peak separation of Ni L_3-edge in rare-earth nickelate is considered as a result of a decrease in Δ [43, 63, 64]. Fig. 4(f) shows an analysis of the Ni L_3-edge corroborating that a decrease in peak separation, implying a decrease in Δ, with the increase in the thickness of the (LPNSE)NO films. According to earlier cluster calculations [43, 63, 64], this decrease of L_3 peak separation by 0.3 eV would correspond to a decrease of Δ by 1 eV. A comparison between the OER activity and L_3 peak separation for our 15, 30 and 75 uc (LPNSE)NO thin films is shown in Fig. 4(g), which clearly shows that a decrease in Δ results higher OER activity.

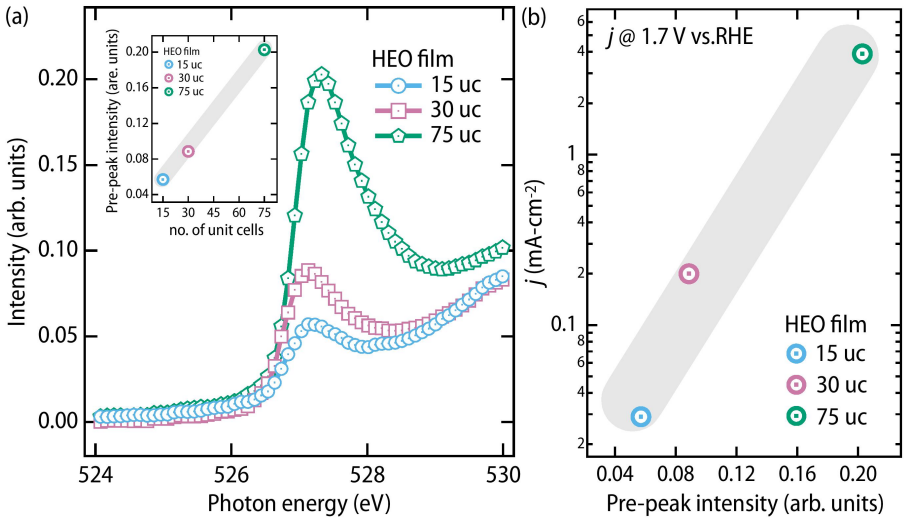

FIG. 5. **O K-edge X-ray absorption spectroscopy.** (a) The pre-peak of Oxygen K-edge XAS spectra for 15, 30, and 75 uc (LPNSE)NO films. The pre-peak intensity as a function of the thickness of the film has been shown in the inset. (b) The current density as a function of the pre-peak intensity of the O K-edge, which is a measure of the covalency between O $2p$ and Ni $3d$ states. The y-axis is in the log scale.

The decrease in Δ with the increasing thickness should enhance the hybridization between O $2p$ and Ni $3d$ states. To check how the covalency affects OER activity of (LPNSE)NO films, we have measured O K-edge XAS. A pre-peak around 527.5 eV (Fig. 5(a)) arises due to the $d^8\underline{L} \rightarrow \underline{c}d^8$ transition ($\underline{c}$ denotes a core hole in O $1s$ core level). [55, 63, 65, 66]. The inset of Fig. 5(a) shows that the pre-peak intensity, which is a measure of the covalency, increases with the increase in film thickness. Fig. 5(b) demonstrates that an increase in the covalency improves OER activity of (LPNSE)NO films.

The change in the charge transfer energy Δ as a function of film thickness is related to the change in the Madelung potential difference (δV_M) between Ni and O as the Δ is microscopically related [67] with the electron affinity of oxygen [$I(\mathrm{O}^{2-})$], ionization potential of Ni^{3+} [$A(\mathrm{Ni}^{3+})$], the Ni and O bond distance ($d_{\mathrm{Ni-O}}$) and δV_M by the relation $\Delta = e\delta V_M$-$A(\mathrm{Ni}^{3+})$+$I(\mathrm{O}^{2-})$-$e^2/d_{\mathrm{Ni-O}}$. An increase in covalency and a decrease in Δ favors charge transfer between Ni^{3+} ions located at the surface and surface adsorbates during the formation of O-O bond [Ni^{3+}-O^{2-}+OH^- $\rightarrow$$\mathrm{Ni}^{2+}$-$\mathrm{OOH}^-$+$e^-$], resulting in higher OER activity with the increase in (LPNSE)NO film thickness [10, 22].

III. CONCLUSION

In summary, we have stabilized single thin films of a HEO and successfully demonstrated them as potential platform for OER activity. We have found that a 75 uc film provides the best results with the current density (1.7 V vs RHE) of 3816 μAcm^{-2} and a Tafel slope of 90 mVdec^{-}1. The thicker films are less effective due to the development of quasi-3D nature of their surface. As the strength of different descriptors are strongly correlated to the thickness, our XAS studies show that the increase of film thickness results a decrease in charge transfer energy, which in turn enhances the covalency between Ni 3d and O 2p and favors better OER activity. Further study with HEOs having multiple elements at the transition metal site will be interesting to elucidate the role of multiple sets of electronic structure parameters in catalytic activity.

[1] H. B. Gray, Nature Chemistry **1**, 7 (2009).

[2] N. S. Lewis and D. G. Nocera, Proceedings of the National Academy of Sciences **103**, 15729 (2006), https://www.pnas.org/doi/pdf/10.1073/pnas.0603395103.

[3] M. W. Kanan and D. G. Nocera, Science **321**, 1072 (2008), https://www.science.org/doi/pdf/10.1126/science.1162018.

[4] S. R. F., Science **324**, 1257 (2009).

[5] M. Armand and J.-M. Tarascon, Nature **451**, 652 (2008).

[6] Y.-C. Lu, Z. Xu, H. A. Gasteiger, S. Chen, K. Hamad-Schifferli, and Y. Shao-Horn, Journal of the American Chemical Society **132**, 12170 (2010), pMID: 20527774, https://doi.org/10.1021/ja1036572.

[7] S. Trasatti, Journal of Electroanalytical Chemistry and Interfacial Electrochemistry **111**, 125 (1980).

[8] K. A. Stoerzinger, L. Qiao, M. D. Biegalski, and Y. Shao-Horn, The Journal of Physical Chemistry Letters **5**, 1636 (2014), pMID: 26270358, https://doi.org/10.1021/jz500610u.

[9] C. C. L. McCrory, S. Jung, J. C. Peters, and T. F. Jaramillo, Journal of the American Chemical Society **135**, 16977 (2013), pMID: 24171402, https://doi.org/10.1021/ja407115p.

[10] J. Suntivich, K. J. May, H. A. Gasteiger, J. B. Goodenough, and Y. Shao-Horn, Science **334**, 1383 (2011), https://www.science.org/doi/pdf/10.1126/science.1212858.

[11] W. T. Hong, K. A. Stoerzinger, Y.-L. Lee, L. Giordano, A. Grimaud, A. M. Johnson, J. Hwang, E. J. Crumlin, W. Yang, and Y. Shao-Horn, Energy Environ. Sci. **10**, 2190 (2017).

[12] W. T. Hong, M. Risch, K. A. Stoerzinger, A. Grimaud, J. Suntivich, and Y. Shao-Horn, Energy Environ. Sci. **8**, 1404 (2015).

[13] J. Suntivich, W. T. Hong, Y.-L. Lee, J. M. Rondinelli, W. Yang, J. B. Goodenough, B. Dabrowski, J. W. Freeland, and Y. Shao-Horn, The Journal of Physical Chemistry C **118**, 1856 (2014), https://doi.org/10.1021/jp410644j.

[14] N.-T. Suen, S.-F. Hung, Q. Quan, N. Zhang, Y.-J. Xu, and H. M. Chen, Chem. Soc. Rev. **46**, 337 (2017).

[15] D. G. Schlom, L.-Q. Chen, X. Pan, A. Schmehl, and M. A. Zurbuchen, Journal of the American Ceramic Society **91**, 2429 (2008).

[16] P. Adiga and K. A. Stoerzinger, Journal of Vacuum Science & Technology A **40**, 010801 (2022), https://doi.org/10.1116/6.0001429.

[17] A. Fernandez, L. Caretta, S. Das, C. Klewe, D. Lou, E. Parsonnet, R. Gao, A. Luo, P. Shafer, and L. W. Martin, Advanced Energy Materials **11**, 2102175 (2021), https://onlinelibrary.wiley.com/doi/pdf/10.1002/aenm.202102175.

[18] A. R. Burton, R. Paudel, B. Matthews, M. Sassi, S. R. Spurgeon, B. H. Farnum, and R. B. Comes, J. Mater. Chem. A **10**, 1909 (2022).

[19] J. R. Petrie, V. R. Cooper, J. W. Freeland, T. L. Meyer, Z. Zhang, D. A. Lutterman, and H. N. Lee, Journal of the American Chemical Society **138**, 2488 (2016), pMID: 26866808, https://doi.org/10.1021/jacs.5b11713.

[20] L. Wang, K. A. Stoerzinger, L. Chang, X. Yin, Y. Li, C. S. Tang, E. Jia, M. E. Bowden, Z. Yang, A. Abdelsamie, L. You, R. Guo, J. Chen, A. Rusydi, J. Wang, S. A. Chambers, and Y. Du, ACS Applied Materials & Interfaces **11**, 12941 (2019), https://doi.org/10.1021/acsami.8b21301.

[21] C. Hu, X. Wang, T. Yao, T. Gao, J. Han, X. Zhang, Y. Zhang, P. Xu, and B. Song, Advanced Functional Materials **29**, 1902449 (2019), https://onlinelibrary.wiley.com/doi/pdf/10.1002/adfm.201902449.

[22] J. Liu, E. Jia, L. Wang, K. A. Stoerzinger, H. Zhou, C. S. Tang, X. Yin, X. He, E. Bousquet, M. E. Bowden, A. T. S. Wee, S. A. Chambers, and Y. Du, Advanced Science **6**, 1901073 (2019), https://onlinelibrary.wiley.com/doi/pdf/10.1002/advs.201901073.

[23] L. Wang, K. A. Stoerzinger, L. Chang, J. Zhao, Y. Li, C. S. Tang, X. Yin, M. E. Bowden, Z. Yang, H. Guo, L. You, R. Guo, J. Wang, K. Ibrahim, J. Chen, A. Rusydi, J. Wang, S. A. Chambers, and Y. Du, Advanced Functional Materials **28**, 1803712 (2018), https://onlinelibrary.wiley.com/doi/pdf/10.1002/adfm.201803712.

[24] C. Baeumer, J. Li, Q. Lu, A. Y.-L. Liang, L. Jin, H. P. Martins, T. Duchoň, M. Glöß, S. M. Gericke, M. A. Wohlgemuth, M. Giesen, E. E. Penn, R. Dittmann, F. Gunkel, R. Waser, M. Bajdich, S. Nemšák, J. T. Mefford, and W. C. Chueh, Nature Materials **20**, 674 (2021).

[25] R. Sankannavar, K. C. Sandeep, S. Kamath, A. K. Suresh, and A. Sarkar, Journal of The Electrochemical Society **165**, J3236 (2018).

[26] Y. Wang, C. Huang, K. Chen, Y. Zhao, J. He, S. Xi, P. Chen, X. Ding, X. Wu, Q. Kong, X. An, F. Raziq, X. Zu, Y. Du, H. Xiao, K. H. Zhang, and L. Qiao, ACS Applied Materials & Interfaces **13**, 58566 (2021), pMID: 34852196, https://doi.org/10.1021/acsami.1c16885.

[27] B. Murty, J. Yeh, S. Ranganathan, and P. Bhattacharjee, in *High-Entropy Alloys (Second Edition)*, edited by B. Murty, J. Yeh, S. Ranganathan, and P. Bhattacharjee (Elsevier, 2019) second edition ed., pp. 13–30.

[28] Y. Zhang, W. Dai, P. Zhang, T. Lu, and Y. Pan, Journal of Alloys and Compounds **868**, 159064 (2021).

[29] W. Huang, J. Zhang, D. Liu, W. Xu, Y. Wang, J. Yao, H. T. Tan, K. N. Dinh, C. Wu, M. Kuang, W. Fang, R. Dangol, L. Song, K. Zhou, C. Liu, J. W. Xu, B. Liu, and Q. Yan, ACS Nano **14**, 17640 (2020), pMID: 33316158, https://doi.org/10.1021/acsnano.0c08571.

[30] Y. Zhang, T. Lu, Y. Ye, W. Dai, Y. Zhu, and Y. Pan, ACS Applied Materials & Interfaces **12**, 32548 (2020), pMID: 32614574, https://doi.org/10.1021/acsami.0c05916.

[31] Z. Sun, Y. Zhao, C. Sun, Q. Ni, C. Wang, and H. Jin, Chemical Engineering Journal **431**, 133448 (2022).

[32] T. X. Nguyen, Y.-C. Liao, C.-C. Lin, Y.-H. Su, and J.-M. Ting, Advanced Functional Materials **31**, 2101632 (2021), https://onlinelibrary.wiley.com/doi/pdf/10.1002/adfm.202101632.

[33] F. Liu, M. Yu, X. Chen, J. Li, H. Liu, and F. Cheng, Chinese Journal of Catalysis **43**, 122 (2022).

[34] S. Zhao, H. Wu, R. Yin, X. Wang, H. Zhong, Q. Fu, W. Wan, T. Cheng, Y. Shi, G. Cai, C. Jiang, and F. Ren, Journal of Alloys and Compounds **868**, 159108 (2021).

[35] C. Duan, X. Li, D. Wang, Z. Wang, H. Sun, R. Zheng, and Y. Liu, Sustainable Energy Fuels **6**, 1479 (2022).

[36] Y. Gu, A. Bao, X. Wang, Y. Chen, L. Dong, X. Liu, H. Pan, Y. Li, and X. Qi, Nanoscale **14**, 515 (2022).

[37] M. L. Medarde, Journal of Physics: Condensed Matter **9**, 1679 (1997).

[38] G. Catalan, Phase Transitions **81**, 729 (2008), https://doi.org/10.1080/01411590801992463.

[39] S. Middey, J. Chakhalian, P. Mahadevan, J. W. Freeland, A. J. Millis, and D. D. Sarma, Annual Review of Materials Research **46**, 305 (2016).

[40] S. Catalano, M. Gibert, J. Fowlie, J. Íñiguez, J.-M. Triscone, and J. Kreisel, Reports on Progress in Physics **81**, 046501 (2018).

[41] J. B. Torrance, P. Lacorre, A. I. Nazzal, E. J. Ansaldo, and C. Niedermayer, Phys. Rev. B **45**, 8209 (1992).

[42] A. V. Boris, Y. Matiks, E. Benckiser, A. Frano, P. Popovich, V. Hinkov, P. Wochner, M. Castro-Colin, E. Detemple, V. K. Malik, C. Bernhard, T. Prokscha, A. Suter, Z. Salman, E. Morenzoni, G. Cristiani, H.-U. Habermeier, and B. Keimer, Science **332**, 937 (2011), http://www.sciencemag.org/content/332/6032/937.full.pdf.

[43] J. Liu, S. Okamoto, M. van Veenendaal, M. Kareev, B. Gray, P. Ryan, J. W. Freeland, and J. Chakhalian, Phys. Rev. B **83**, 161102 (2011).

[44] K. D. C., W. I., N. F., UchidaM., AdamoC., ZhuS., HeX., BozovicI., S. G., and S. M., Nat Nano **9**, 443 (2014).

[45] Y. E. Suyolcu, K. Fürsich, M. Hepting, Z. Zhong, Y. Lu, Y. Wang, G. Christiani, G. Logvenov, P. Hansmann, M. Minola, B. Keimer, P. A. van Aken, and E. Benckiser, Phys. Rev. Materials **5**, 045001 (2021).

[46] O. Y. Gorbenko, S. Samoilenkov, I. Graboy, and A. Kaul, Chemistry of materials **14**, 4026 (2002).

[47] R. K. Patel, S. K. Ojha, S. Kumar, A. Saha, P. Mandal, J. W. Freeland, and S. Middey, Applied Physics Letters **116**, 071601 (2020), https://doi.org/10.1063/1.5133710.

[48] H. Guo, Z. Li, L. Zhao, Z. Hu, C. Chang, C.-Y. Kuo, W. Schmidt, A. Piovano, T. Pi, O. Sobolev, D. Khomskii, L. Tjeng, and A. Komarek, Nature communications **9**, 43 (2018).

[49] H. Zheng, J. Zhang, B. Wang, D. Phelan, M. J. Krogstad, Y. Ren, W. A. Phelan, O. Chmaissem, B. Poudel, and J. F. Mitchell, Crystals **9** (2019), 10.3390/cryst9070324.

[50] A. R. Kaul, O. Y. Gorbenko, and A. A. Kamenev, Russ. Chem. Rev. **73**, 861 (2004).

[51] G. Mattoni, P. Zubko, F. Maccherozzi, A. van der Torren, D. B. Boltje, M. Hadjimichael, N. Manca, S. Catalano, M. Gibert, Y. Liu, and et al., Nature Communications **7**, 13141 (2016).

[52] K. W. Post, A. S. McLeod, M. Hepting, M. Bluschke, Y. Wang, G. Cristiani, G. Logvenov, A. Charnukha, G. X. Ni, P. Radhakrishnan, M. Minola, A. Pasupathy, A. V. Boris, E. Benckiser, K. A. Dahmen, E. W. Carlson, B. Keimer, and D. N. Basov, Nature Physics **14**, 1056 (2018).

[53] N. Palina, L. Wang, S. Dash, X. Yu, M. B. H. Breese, J. Wang, and A. Rusydi, Nanoscale **9**, 6094 (2017).

[54] L. Wang, S. Ju, L. You, Y. Qi, Y.-w. Guo, P. Ren, Y. Zhou, and J. Wang, Scientific Reports **5**, 18707 (2015).

[55] J. Liu, M. Kargarian, M. Kareev, B. Gray, P. J. Ryan, A. Cruz, N. Tahir, Y.-D. Chuang, J. Guo, J. M. Rondinelli, J. W. Freeland, G. A. Fiete, and J. Chakhalian, Nat Commun **4**, 2714 (2013).

[56] M. Kotiuga, Z. Zhang, J. Li, F. Rodolakis, H. Zhou, R. Sutarto, F. He, Q. Wang, Y. Sun, Y. Wang, N. A. Aghamiri, S. B. Hancock, L. P. Rokhinson, D. P. Landau, Y. Abate, J. W. Freeland, R. Comin, S. Ramanathan, and K. M. Rabe, Proceedings of the National Academy of Sciences **116**, 21992 (2019).

[57] J. Zaanen, G. A. Sawatzky, and J. W. Allen, Phys. Rev. Lett. **55**, 418 (1985).

[58] S. Nimkar, D. D. Sarma, H. R. Krishnamurthy, and S. Ramasesha, Phys. Rev. B **48**, 7355 (1993).

[59] S. Middey, D. Meyers, S. K. Ojha, M. Kareev, X. Liu, Y. Cao, J. W. Freeland, and J. Chakhalian, Phys. Rev. B **98**, 045115 (2018).

[60] J. Suntivich, H. A. Gasteiger, N. Yabuuchi, H. Nakanishi, J. B. Goodenough, and Y. Shao-Horn, Nature Chemistry **3**, 546 (2011).

[61] S. R. Barman, A. Chainani, and D. D. Sarma, Phys. Rev. B **49**, 8475 (1994).

[62] V. Bisogni, S. Catalano, R. J. Green, M. Gibert, R. Scherwitzl, Y. Huang, V. N. Strocov, P. Zubko, S. Balandeh, J.-M. Triscone, G. Sawatzky, and T. Schmitt, Nature Communications **7**, 13017 (2016).

[63] J. W. Freeland, M. van Veenendaal, and J. Chakhalian, Journal of Electron Spectroscopy and Related Phenomena **208**, 56 (2016), special Issue: Electronic structure and function from state-of-the-art spectroscopy and theory.

[64] D. Meyers, S. Middey, M. Kareev, M. van Veenendaal, E. J. Moon, B. A. Gray, J. Liu, J. W. Freeland, and J. Chakhalian, Phys. Rev. B **88**, 075116 (2013).

[65] M. Medarde, A. Fontaine, J. L. García-Muñoz, J. Rodríguez-Carvajal, M. de Santis, M. Sacchi, G. Rossi, and P. Lacorre, Phys. Rev. B **46**, 14975 (1992).

[66] S. Middey, P. Rivero, D. Meyers, M. Kareev, X. Liu, Y. Cao, J. W. Freeland, S. Barraza-Lopez, and J. Chakhalian, Sci. Rep. **4**, 6819 (2014).

[67] M. Imada, A. Fujimori, and Y. Tokura, Rev. Mod. Phys. **70**, 1039 (1998).

EXPERIMENTAL METHODS

All the films were grown by a Neocera pulsed laser deposition system and the growths were monitored in situ by a high pressure RHEED from the Staib Instruments, Germany. The X-ray diffraction patterns were recorded by laboratory-based Rigaku Smartlab X-ray diffractometer to confirm the single phase of all the thin films. The electrical transport measurements were done in four probe Van der Pauw geometry using an ARS closed cycle cryostat and Keithley 6221 current source and Keithley 2182 A nanovoltmeter. X-ray absorption spectroscopy at Ni $L_{3,2}$ and O-K edges using bulk-sensitive total fluorescence yield mode were performed at the 4.0.2 beam line of the Advanced Light Source (ALS), Lawrence Berkeley National Laboratory, Berkeley, USA.

All Electrochemical measurements were performed in a three-electrode set-up using CHI 660A electrochemical analyzer (CHI Instruments, USA). The high entropy oxides grown on NGO substrate work as the working electrodes. Mercury-mercuric oxide (MMO) is used as a reference electrode which is converted to reversible hydrogen electrode (RHE) and carbon rod is utilized as the counter electrode. The OER testing is performed in 0.1 M potassium hydroxide (KOH) electrolyte. Linear scan voltammetry (LSV) was performed with a scan rate of 10mVsec^{-1}. The stability test of the electrodes are carried out by measuring the current over time period at a constant voltage. The Tafel slopes were determined by taking the linear region of polarization curves, which fitted according to Butler-Volmer equation given by $\eta = b \log j + a$, where η, j, a, and b are over potential, current density, intercept, and Tafel slope, respectively.

ACKNOWLEDGEMENTS

The authors acknowledge XRD facilities at the Department of Physics, IISc Bangalore. SM acknowledges DST Nanomission grant (DST/NM/NS/2018/246) and Infosys Foundation, Bangalore for financial support. This research used resources of the Advanced Light Source, which is a Department of Energy Office of Science User Facility under Contract No. DE-AC02-05CH11231.

COMPETING INTERESTS

The authors declare no competing interests.

Supplementary Material

S1. Post OER characterization by XRD and transport measurements:

The oxygen evolution reaction (OER) may damage the sample through formation of metal oxide/hydroxide/oxyhydroxide. Hence, checking the status of the samples after the OER measurement is absolutely necessary. In this regard, we have checked the X-ray diffraction (XRD) and transport properties after the electrocatalysis. Fig. S1(a) shows a comparison between the XRD scan of the 45 uc $(La_{0.2}Pr_{0.2}Nd_{0.2}Sm_{0.2}Eu_{0.2})NiO_3$ (HEO) thin film before and after the oxygen evolution reaction. The film peaks have very similar intensity, demonstrating that the HEO phase is intact upon electrocatalysis. Again, the overlapping thickness fringes confirm high quality of the film is preserved without any film degradation after the OER process. Similar comparison of the transport data of the 45 uc film has been shown in Fig. S1(b). The resistivity data measured after the OER still shows a metal to insulator transition (MIT), similar to the pristine case. A small change of the peak position in the XRD and a deviation of the metal-insulator transition temperature in the transport measurement can be attributed to the some changes within the surface of the film during OER. Overall, the structural and electronic properties are very similar before and after the OER measurements.

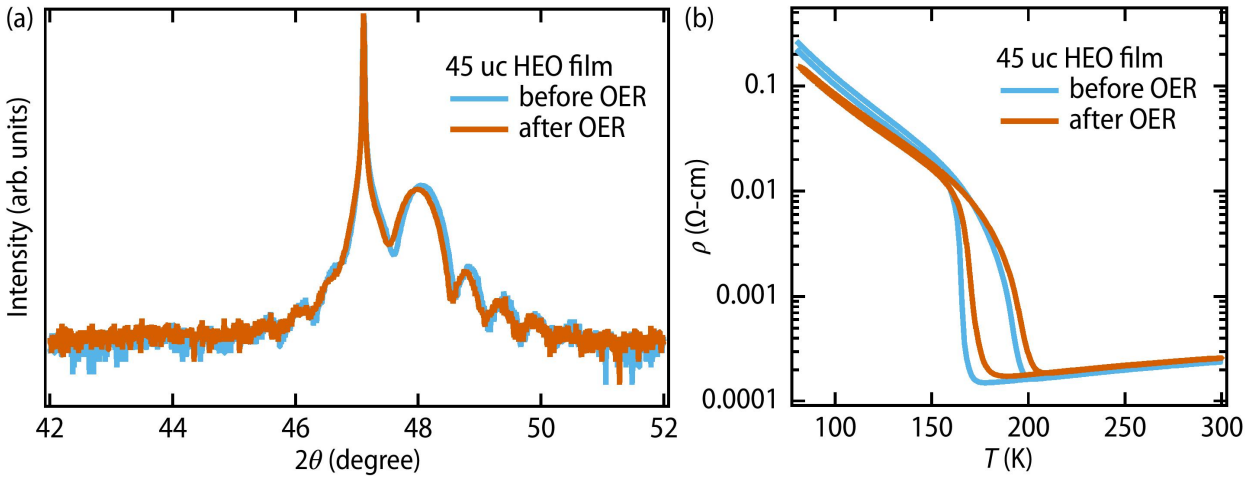

FIG. S1. (a) The XRD scan around the NdGaO3 (002)pc and (b) the resistivity as a function of temperature of the 45 uc HEO thin film before and after the OER electrocatalysis.

S2.Stability test:

If an electrode can keep the activity for a long time, it can be used for large-scale applications. To check the durability of the electrodes, a chronoamperometric experiment was performed at 1.7 V vs. RHE. All the samples are stable (Fig. S2(a)) and the 75 uc thin film shows the highest current density. Fig. S2(b) shows a comparison in the stability data between the 45 uc and 100 uc samples upto 24 hours. The 45 uc thin film, the current density does not go to zero suggesting the durable performance of the electrode for long-term use (the sudden jumps are due to the formation and annihilation of the bubbles during the stability test), whereas the current density decreases with time and became zero after 14 hours for the 100 uc thin film. This instability of the 100 uc film can be ascribed to the poor quality of the 100 uc film (3D growth from the broken streaks in the RHEED pattern and the possibility of phase decomposition) due to higher thickness, which has been discussed in the main text of the paper.

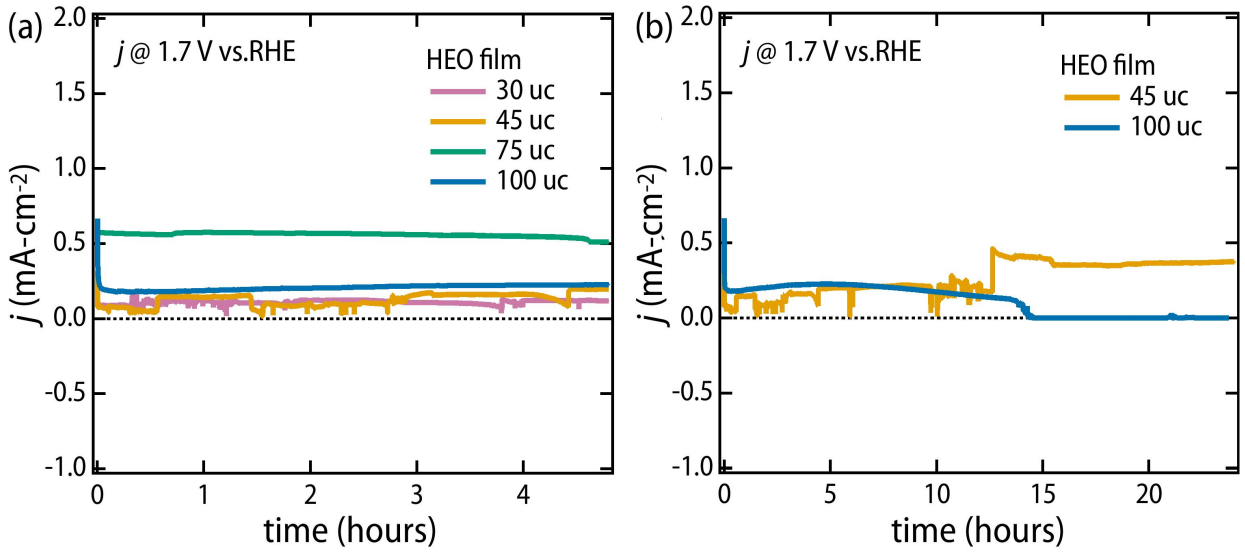

FIG. S2. The chronoamperometric stability experiment of the samples at 1.7 V vs. RHE (a) for 5 hours and (b) the extended data for 24 hours of the 45 uc and 100 uc thin films.